



Multi-shape graph cuts with neighbor prior constraints and its application to lung segmentation from a chest CT volume

Keita Nakagomi^a, Akinobu Shimizu^{a,*}, Hidefumi Kobatake^a, Masahiro Yakami^b, Koji Fujimoto^b, Kaori Togashi^b

^a Tokyo University of Agriculture and Technology, Tokyo, Japan

^b Kyoto University, Kyoto, Japan

ARTICLE INFO

Article history:

Received 9 February 2012

Received in revised form 14 July 2012

Accepted 31 August 2012

Available online 23 September 2012

Keywords:

Graph cuts

Multi-shape

Lung segmentation

Neighbor constraint

CT image

ABSTRACT

This paper presents a novel graph cut algorithm that can take into account multi-shape constraints with neighbor prior constraints, and reports on a lung segmentation process from a three-dimensional computed tomography (CT) image based on this algorithm. The major contribution of this paper is the proposal of a novel segmentation algorithm that improves lung segmentation for cases in which the lung has a unique shape and pathologies such as pleural effusion by incorporating multiple shapes and prior information on neighbor structures in a graph cut framework. We demonstrate the efficacy of the proposed algorithm by comparing it to conventional one using a synthetic image and clinical thoracic CT volumes.

© 2012 Elsevier B.V. All rights reserved.

1. Introduction

Accurate segmentation is a prerequisite for quantitative lung computed tomography (CT) image analysis and also for computer-aided diagnoses. The segmentation method described in this paper will be built in the development of a computer aided diagnosis (CAD) system for a thoracic CT volume. Many CAD systems that detect and/or quantify pathologies require accurate segmentation of the target organ as its initial step. In this paper, we propose a method that aims to accurately extract lungs that contain pathologies such as tumors, emphysema, and diffuse pulmonary disease, as well as pleural effusion. In this study, we included pleural effusion as a segmentation target for the following two reasons: First, the segmentation of pleural effusion is beneficial in diagnosis because the mere existence of pleural effusion is usually symptomatic of pathologies such as tumors, tuberculosis, thoracic empyema, and pneumonia. Its presence, location, and volume are important factors that can assist a physician during diagnosis (Light, 2008). Second, it facilitates the usage of a statistical shape model (SSM) in the segmentation process (Cremers et al., 2007; Heimann and Meinzer, 2009). A pleural effusion is fluid that builds up in a pleural cavity (Fig. 1b), which is space that is usually occupied by the lungs in healthy subjects. Therefore, by considering the

combination of a lung and a pleural effusion as one region, the shape of the region is identical to that of the lungs of a subject not afflicted with pleural effusion. The shape in Fig. 1c, reconstructed from a SSM that learned from subjects without pleural effusion, is beneficial in the segmentation of the region comprising a lung and a pleural effusion.

Many methods for automatically extracting the lung regions from three-dimensional (3D) CT volumes have been proposed (Sluimer et al., 2006). Since a normal lung appears dark in a CT image and is surrounded by denser regions, most methods focus on this contrast information. Although such methods are known to be simple and effective (Hu et al., 2001), they often fail to extract regions affected by pathologies, especially when the pathologies are attached to pleura of the lungs. This is a challenging problem because many pathologies exhibit different properties when compared with normal tissues, and we often find that the region of pathology cannot be recovered by post-processing such as morphological operations or holes filling. In addition, contrast-based methods also fail to extract pleural effusion (Fig. 1d) because it is denser than normal lung tissue.

Other approaches use different features of lungs, such as shape, rather than contrasts to extract lungs with pathologies. Sluimer et al. (2008) proposed a registration-based approach in which a shape template is registered to an input CT volume. They achieved significant improvements in the segmentation of lungs with pathologies, but the algorithm is time-consuming because of the combination of the registration and classification processes. In

* Corresponding author.

E-mail addresses: simiz@cc.tuat.ac.jp (A. Shimizu), kobatake@cc.tuat.ac.jp (H. Kobatake).

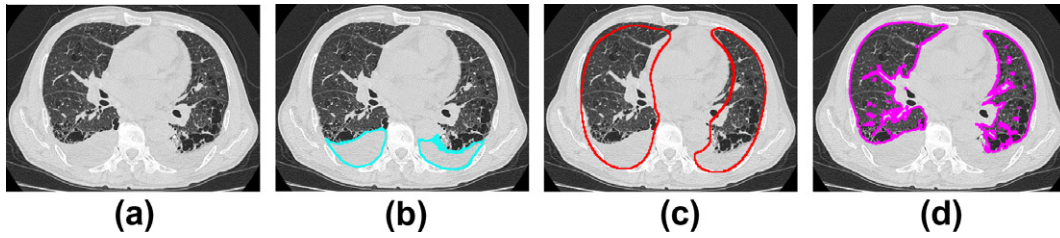


Fig. 1. An example of a case with a pleural effusion: (a) Original image, (b) Pleural effusion (light-blue line), (c) An example of shapes reconstructed by an SSM trained from subjects without pleural effusion (red line), and (d) Segmentation result of contrast-based method (purple line). (For interpretation of the references to color in this figure legend, the reader is referred to the web version of this article.)

addition, it suffers from low accuracy in segmentation due to errors in registration and classification. Kido and Tsunomori (2009) proposed another registration based method using a template obtained from a normal case. Two step matching improved the performance of the case with severe plural effusion but still suffered from error in the registration. Hua et al. (2011) proposed a method that combines the classification process with a graph-search algorithm. The method has been shown to be effective in cases containing pathologies. However, the construction of the graph is limited to a narrow band around the pre-segmented lung surface obtained from the gray-value statistics-based method, which might fail in cases with large pathologies. One of the workshops held in conjunction with the Medical Image Computing and Computer Assisted Intervention (MICCAI) conference in 2011 hosted a segmentation challenge called Lobe and Lung Analysis (LOLA). Its goal was to compare methods for (semi-)automatic segmentation of the lungs from chest CT scans. The results of the contest showed that methods based on contrast information got high marks and proved effective in segmentation of the lungs. Although their dataset covered various pathologies of the lungs, the target region to be segmented did not include pleural effusion. Therefore, our target is different from that of LOLA 2011.

With regards to the segmentation of pleural effusion, a few of methods have been proposed in the past. Yao et al. (2009) proposed a stepwise method to extract pleural effusion using the pre-segmented lung surface obtained from the gray-value statistics-based process followed by visceral and parietal pleura detection based on active contour models. Their process could not extract both lung and pleural effusion simultaneously, which is different from our approach. Furthermore, the segmentation process fails when the lung is not extracted correctly. In addition, the continuity of the pleura surface between slices was not maintained due to the use of 2D active contour models. Moreover, their experiment was limited to cases with pleural effusion.

In this paper, we propose an s - t graph cut-based (Boykov and Funka-Lea, 2006) segmentation algorithm, with multiple-shape and neighbor priors (i.e., the aorta and the body cavity), which can optimize the energy function defined in an entire CT volume. A graph cut algorithm is a noteworthy development in which the global minimum for a sub-modular function of a binary label problem is guaranteed. Furthermore, a number of researchers have introduced a shape prior into the graph cut approach in order to obtain accurate segmentation (Freedman and Zhang, 2005; Slabaugh and Unal, 2005; Funka-Lea et al., 2006). These papers propose several ways in which a general shape constraint such as an ellipse, a star, or an arbitrary shape defined by the user can be incorporated. Shimizu et al. (2010) combined a patient-specific shape estimated by a statistical shape model (SSM) with graph cuts. However, all of the above methods consider single-shape information only, which might be different from the true shape, thus resulting in inadequate performance. Combining multiple-shape information helps to reduce such differences. Linguraru et al.

(2012) proposed a shape-based energy computed by the Parzen window method which is a population statistic based method but the combinatorial problem of multiple shape information remains unsolved. In addition to such shape a priori, neighbor constrained energy was also introduced in a graph cut approach by Shimizu et al. (2010) to boost segmentation performance. It incorporated a prior knowledge about the region to be segmented based on neighbor structures (i.e. the dorsal ribs) and was shown to be effective in segmentation. However, the energy still suffered from low accuracy in lung segmentation as a result of the various patterns in shape, especially in the area close to the aorta.

The major contribution of this paper is the proposal of a graph cut-based segmentation algorithm that improves lung segmentation by incorporating multiple shapes and prior information on neighbor structures of the lungs (i.e., the aorta and the body cavity). In this paper, we extend the term “lungs” to refer not only to the region of normal lung tissues, but also to the regions of pathological abnormality, including pleural effusion. By permitting a graph cut algorithm to consider multiple shape priors, our method improves lung segmentation without relying too strongly on a single shape prior. Moreover, we introduce novel neighbor constrained energy terms to extract the lungs with various shapes and appearances caused by differences in shape and pathologies, including pleural effusion.

In the remainder of this paper, we will explain the details of our proposed method and demonstrate its efficacy using the experimental results of a synthetic image and 97 thoracic CT volumes taken in daily clinical routine. These CT volumes contain pulmonary diseases such as a lung tumor, emphysema, diffuse pulmonary disease, and a pleural effusion; and include both non-contrast and contrast CT volumes. The quantitative evaluation is performed using an average of the Jaccard Index of the lungs and the sensitivity of a lesion attached to the chest wall. This is followed by a discussion of the effectiveness of our proposed method.

2. Proposed segmentation framework

2.1. Single-shape graph cuts

A graph cut formulates a segmentation problem as an energy minimization problem (Boykov and Funka-Lea, 2006). Given a set of voxels, P , and a set of labels, $L = \{0, 1\}$, the goal is to assign a label $l \in L$ to each $p \in P$. Let A_p denote a label assigned to voxel p , and let $\mathbf{A} = \{A_1, A_2, \dots, A_p, \dots, A_{|P|}\}$ be the collection of all label assignments. This gives the energy function:

$$E(\mathbf{A}) = \lambda \cdot R(\mathbf{A}) + B(\mathbf{A}) = \lambda \cdot \sum_{p \in P} R_p(A_p) + \sum_{\{p,q\} \in N} B_{p,q} \cdot \delta_{A_p \neq A_q} \quad (1)$$

There are two types of energy terms in Eq. (1). The first term is called the “data term”, which expresses a penalty for assigning label A_p to voxel p . Generally, we use the negative log likelihood of the

gray value for this term. The second term, $B_{p,q}$, is called the “boundary term”. This term expresses a penalty for assigning labels A_p and A_q to the two neighboring voxels, p and q . This term originally relies on a gradient value between voxels p and q . The set N is a collection of neighboring voxel pairs. The function δ is 1 if $A_p \neq A_q$, and 0 otherwise. The coefficient λ in the equation is a constant value balancing the two terms. In addition, if a voxel is known to belong to an “object” or “background” prior to the segmentation, a graph cut algorithm can incorporate such a priori knowledge as “object” or “background” seed, in which the voxel is labeled the same as the seed. In the following paragraphs, we briefly review the “single-shape graph cuts” in (Shimizu et al., 2010).

One of the contributions of this paper is the proposal of an energy term that can penalize the segmentation boundary based on a patient-specific shape. The following shape-constrained term, $S_{p,q}$, was introduced in the boundary term:

$$E(\mathbf{A}) = \lambda \cdot \sum_{p \in P} R_p(A_p) + \sum_{\{p,q\} \in N} \{B_{p,q} + S_{p,q}\} \cdot \delta_{A_p \neq A_q} \quad (2)$$

$$S_{p,q} = \sqrt{\frac{1 - \cos(\theta)}{2}} \quad (3)$$

where θ represents the angle between a vector connecting voxels p and q and a gradient vector of a signed distance $\varphi(p)$ from the boundary of a given shape. This term encourages the energy to be low when the direction of a vector connecting p and q is similar to that of the gradient vector of $\varphi(p)$. As a result, the surface normals of an extracted region tend to be parallel to those of the given shape and the extracted region is similar to the shape.

Although the shape-constrained energy term $S_{p,q}$ has been shown to be effective, the algorithm still suffers from low accuracy, especially with test data. A patient-specific shape prior was estimated using an SSM beforehand. The estimation process works quite well for most cases, but it is still a challenging problem when dealing with test data in which an organ's shape is different from that found in a training dataset. Therefore, using only a single shape is risky. In this case, a collection of multiple shapes could account for the shape in the test dataset. As a result, we propose a framework that can take multiple shape constraints into account.

2.2. Multi-shape graph cuts

This subsection presents a graph cut-based segmentation algorithm that can solve the problem encountered when multiple shape priors are combined. Unlike conventional graph cut algorithms, which deal with binary label problems, we now consider multiple-shape priors, or multiple labels. Let a set, L , be a label set $\{0, 1, 2, \dots, n\}$ in which each label corresponds to a prior shape. Fig. 2 shows examples of labels, each with its original shape. Our goal is to develop an algorithm that will select an optimal shape prior at each voxel by minimizing the energy function, including the shape energy, of Eq. (4).

$$E_{\text{shape}} = \sum_{\{p,q\} \in N} S_{p,q} \cdot \delta \quad (4)$$

$$S_{p,q} = \text{MIN} \left(\sqrt{\frac{1 - \cos(\theta_{A_p})}{2}}, \sqrt{\frac{1 - \cos(\theta_{A_q})}{2}} \right)$$

where θ_{A_p} represents the angle between a vector connecting voxels p and q , and a gradient vector of a signed distance $\varphi_{A_p}(p)$ from the boundary of a shape corresponding to a label $A_p \in L$. Here, δ is a function that equals 0 when the neighboring voxels belong to the same class, and 1 otherwise. Note that there are two classes, a lung (“object”) class and background class in our problem.

Ideally, it is best to solve a multi-label problem in one step. When labels in a set L have certain relationships to each other, such

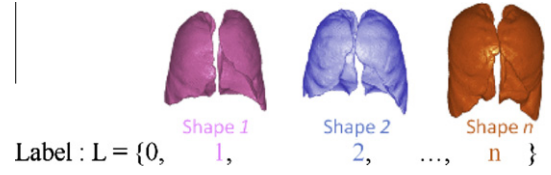


Fig. 2. A set of labels with their corresponding shapes.

as containment and attraction relationships, there are algorithms that guarantee a global optimum of the multi-label problem (Ishikawa, 2003; Delong and Boykov, 2009). However, when labels do not have such relationships, as in our case, there is no algorithm that can handle problems in this manner. Instead, researchers use an approximation algorithm that employs an iterative scheme, such as alpha-expansion (Boykov et al., 2001) or fusion move (Lempitsky et al., 2010). These methods sequentially propose a label against the current label at each voxel. An important difference between the two algorithms is that the fusion move algorithm can simultaneously propose multiple labels in varying locations, but the alpha-expansion algorithm cannot. As explained in detail below, our algorithm proposes labels that differ by location so as to ensure the sub-modularity of the shape energy of Eq. (4). Consequently, we employ the fusion move algorithm, which iteratively solves a series of problems between a set of current labels and a set of proposed labels using the QPBO min-cut algorithm (Rother et al., 2007).

Let X^{cur} be a collection of current labels and X^{pro} be a set of proposed labels. Note that both X^{cur} and X^{pro} include multiple labels, each of which corresponds to a prior shape. In order to ensure the sub-modularity of the shape energy, we divide the current labels into object labels and background labels. First, the fusion move algorithm proposes an object label l against voxels whose current labels X^{cur} are background, and proposes the same labels as current for other voxels ($X^{\text{pro}} \leftarrow X^{\text{cur}}$). The QPBO min-cut algorithm can find a combinatorial optimal solution of labels, or shapes. This step can reduce false negatives, but cannot deal with false positives because the proposed label of a voxel labeled as object currently is the same as X^{cur} , which ensures the sub-modularity proven in Appendix A. The second step focuses on false positives based on the same analogy. It proposes a background label l against voxels whose current labels X^{cur} are objects. To differentiate between background labels and object labels, negative labels are introduced to represent background labels. Eventually, the set of labels L is extended to $L = \{1, -1, 2, -2, \dots, n, -n\}$, where the absolute value of a label refers to the number of a shape, and its sign represents either object or background. The QPBO min-cut algorithm can again find combinatorial optimal solutions of labels in the second step of the background proposal. We iterate a pair of object and background proposals by changing a label, or a prior shape. The algorithm stops the iteration process when no label changes or when it reaches the maximum number of iterations defined by the user. Our method is summarized in Algorithm 1 and the differences over the single-shape graph cuts are listed in Table 1.

Table 1
Differences between single-shape and multi-shape graph cuts.

	Single-shape	Multi-shape
Number of shapes	1	n
Labels in A	binary	multiple labels ($2n$)
“Object” label(s)	1	$\{1, 2, \dots, n\}$
“Background” label(s)	0	$\{-1, -2, \dots, -n\}$

Algorithm 1. Multi-shape graph cuts

Input: a set of labels L, X^{cur}
Result: segmented regions
Initialize $X^{\text{cur}} = \{-1, \dots, -1\}$
Repeat
 for each $l \in L$ **do**
 Generate a set of labels X^{pro} where either l or an element of X^{cur} is assigned at each voxel
 $X^{\text{cur}} \leftarrow X^{\text{cur}} \odot X^{\text{pro}} \odot$: fusion move operator (Lempitsky et al., 2010)
 end for
until Convergence: no label changes or the maximum number of iterations is reached

2.3. Neighbor constrained energy terms

As stated in the introduction, neighbor constrained energy was proposed as a new data term for graph cuts by Shimizu et al. (2010). The objective was to increase accuracy in segmentation using prior knowledge about the relationship between a target object and background. Here, the term “neighbor” refers to the surrounding anatomical structures of a target organ and “neighbor constrained energy” refers to an energy term that is defined using a label of the surrounding anatomical structures. One of the advantages of using a neighbor constrained energy term is that it provides effective, consistent information about an organ when the boundary of the organ is unclear due to pathological abnormalities. An example of a neighbor structure is a rib, which is effective in segmenting the lungs with pathological abnormalities attached to the chest wall. The neighbor-constrained term proposed by Shimizu et al. (2010) implies that the voxels inside the thoracic area surrounded by the dorsal ribs are more likely to be segmented as the lung. However, we found experimentally that the energy still suffered from a low accuracy in segmentation of the lung as a result of various patterns in shape, especially in the area near the aorta. Therefore, we propose a novel neighbor-constrained energy term concerning the aorta region. The following equation shows a neighbor-constrained term defined in a general fashion so as to be applicable to other neighboring anatomical structures.

$$NB_p(A_p) = \begin{cases} L_{nb}(p) & (\text{if } A_p > 0) \\ -L_{nb}(p) & (\text{if } A_p < 0) \end{cases} \quad (5)$$

where $L_{nb}(p)$ represents a binary label given to a voxel p , 1 for neighbor structures of the lungs and 0 for other regions. This energy term penalizes a voxel to be labeled as lung when the voxel is known to belong to a neighboring structure prior to the lung segmentation and drive the voxel to be labeled as background. In our study, we do a rough extraction of an aorta region using a conventional graph cut algorithm based on a prior probability and appearance of the aorta learned from training data, as explained in Section 3. Subsequently, we use the extracted region as a neighbor structure.

In addition to the above new term, we also propose another novel boundary term for neighbor constraint. Suppose that the boundary of a neighbor structure, NBb , is highly reliable and coincides with the true boundary of a target organ in part. The following equation gives a penalty when the segmentation boundary between voxels p and q does not coincide with the reliable boundary extracted in advance.

$$\delta_{NBb_p=NBb_q} = \begin{cases} 1 & (\text{if } NBb_p = NBb_q) \\ 0 & (\text{if } NBb_p \neq NBb_q) \end{cases} \quad (6)$$

where NBb_p represents a label at voxel p . Intuitively, the above energy term is similar in nature to a “perforated line” because it guides the graph cut algorithm to obtain the same cut at the reliable boundary. We will give an example of a body cavity whose boundary should be equal to lung boundaries except for mediastinal space (see Fig. 3b and c) in this paper. We first extract the boundary of a body cavity using a conventional graph cut algorithm based on the bone region before the lung segmentation, which will be explained in detail in the next section. Note that the segmentation is easy and the result is highly reliable as the shape of the body cavity is simple. In this study, we use the labeled image of the body cavity, NBb , as the prior knowledge for segmentation of the lungs.

The result of graph cut segmentation depends not only on the individual energy term but also on the weight for combination of the terms. The coefficient λ of Eq. (1) is the weight balancing a data term and a boundary term, which is usually a constant. However, in a local region, one term can be more crucial than the other. Therefore, we introduce an adaptive weight, $\lambda_{NB}(p)$, multiplied to a data term, where the weight changes according to the position, as in Eq. (7).

$$\lambda_{NB}(p) = \begin{cases} \lambda \cdot \left(1.0 - \frac{1.0}{1.0 + \exp(|\text{Dist}(p)| - b)}\right) & (\text{if } \text{Dist}(p) \leq 0.0) \\ \lambda & (\text{if } \text{Dist}(p) > 0.0) \end{cases} \quad (7)$$

where $\text{Dist}(p)$ represents a signed distance from the boundary of the body cavity, a negative distance for inside and positive for outside, and b is a parameter. We empirically set the value of $b = 10$ [mm]. The above adaptive weight implies that the boundary term has more significance over a data term at local regions near the boundary of a body cavity (see Fig. 3d).

2.4. Energy function used in a lung segmentation process

This subsection explains the energy function used in this study. The final energy used for our proposed method, neighbor constrained multi-shape graph cuts, is given in Eq. (8), in which a probabilistic atlas-based data term, $Atlas_p(A_p)$ (Linguraru et al., 2010) is combined with the energies outlined in Sections 2.2 and 2.3.

$$E(\mathbf{A}) = \sum_{p \in P} \lambda_{NB}(p) \cdot \{R_p(A_p) + Atlas_p(A_p) + NB_p(A_p)\} + \sum_{\{p,q\} \in N} \{B_{p,q} + S_{p,q}\} \cdot \delta_{A_p \cdot A_q < 0} \cdot \delta_{NBb_p=NBb_q} \quad (8)$$

$$R_p(A_p) = \begin{cases} \Pr(\text{“bkg”} | I_p) & (\text{if } A_p > 0) \\ \Pr(\text{“obj”} | I_p) & (\text{if } A_p < 0) \end{cases} \quad (9)$$

$$Atlas_p(A_p) = \begin{cases} 1.0 - P_{atlas}(p) & (\text{if } A_p > 0) \\ P_{atlas}(p) & (\text{if } A_p < 0) \end{cases} \quad (10)$$

where the posterior probabilities of Eq. (9) given the intensity value I_p at a voxel p are computed under the assumption of uniform prior probability and Gaussian likelihood with parameters calculated from training data. $P_{atlas}(p)$ represents the prior probability of the lungs at voxel p calculated from lung labels in training data after the spatial standardization explained in next section. The function δ for boundary terms is as defined in Eq. (11) below.

$$\delta_{A_p \cdot A_q < 0} = \begin{cases} 1 & (\text{if } A_p \cdot A_q < 0) \\ 0 & (\text{if } A_p \cdot A_q > 0) \end{cases} \quad (11)$$

Since positive labels represent an object class and negative labels represent a background class, the above equation is intrinsically the same as the δ in Eq. (1).

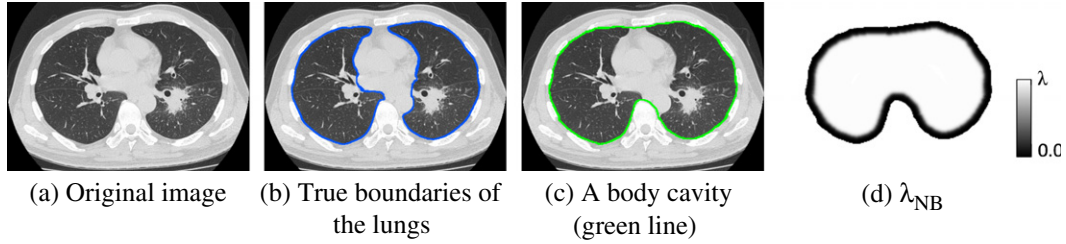


Fig. 3. Relationship between the lungs, body cavity, and adaptive weights computed from the body cavity: (a) Original image, (b) True boundaries of the lungs, (c) A body cavity (green line), and (d) λ_{NB} . (For interpretation of the references to color in this figure legend, the reader is referred to the web version of this article.)

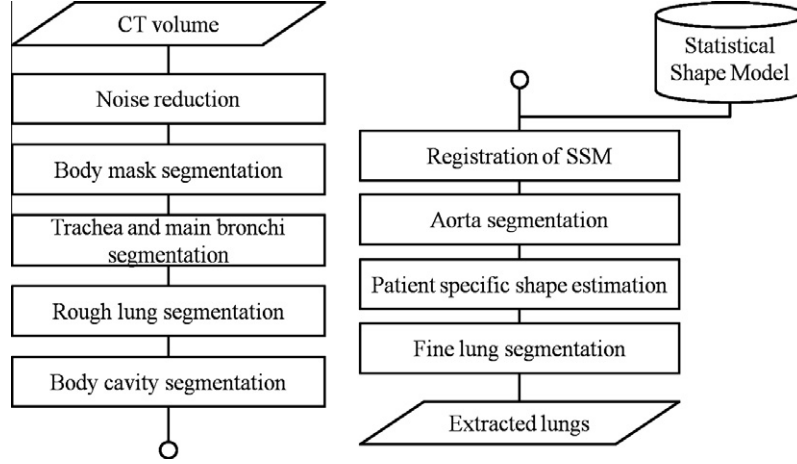


Fig. 4. Flowchart for our lung segmentation system.

3. Lung segmentation system

Fig. 4 presents a flowchart of the lung segmentation system.

The input to the system is a thoracic CT volume and the first step is a noise reduction process based on median filtering (mask size: $3 \times 3 \times 3$). Next, body mask segmentation is performed based on a thresholding (-200 [HU]) followed by morphological operations (opening, radius = 3.0 [mm]) and a hole filling process. Third, we extract a trachea and main bronchi based on region growing so as to avoid false positives in these areas. The seed regions of this process are generated by a thresholding (-950 [HU]) and the extracted regions are excluded from the body mask. The fourth process is a rough extraction of the lungs using a thresholding (-300 [HU]). The two connected components with the largest volumes are defined and forwarded to the patient specific shape estimation process as well as to the fine lung segmentation process where the components are used as object seeds in graph cuts. Here all these parameters, such as threshold values, filter sizes as well as parameters in the following process were decided experimentally using training data.

The fifth process is body cavity extraction, which is used to place landmarks for the registration of the SSM of the lungs and aorta, as well as neighbor constraint, NBb, for fine lung segmentation. A single-shape graph cut with the following energy function is performed to extract the body cavity. Since bones can be used as landmarks to determine the boundary of a body cavity, we apply non-linear transformation of CT values to an input image, where values below 70 [HU] were set to 70 and values over 100 [HU] were clipped at 100 (see Fig. 5b), which is used to compute $B_{p,q}$.

$$E(\mathbf{A}) = \lambda \cdot \sum_{p \in P} R_{body(p)}(A_p) + \sum_{\{p,q\} \in N} \{B_{p,q} + S_{p,q}\} \cdot \delta_{A_p \neq A_q} \quad (12)$$

$$R_{body(p)}(A_p) = \begin{cases} 0.0 & (\text{if } A_p = 1) \\ 0.0 & (\text{if } A_p = 0 \text{ and } D_{muscle}(p) > -10.0[\text{mm}]) \\ 1.0 & (\text{if } A_p = 0 \text{ and } D_{muscle}(p) \leq -10.0[\text{mm}]) \end{cases} \quad (13)$$

where $D_{muscle}(p)$ represents a signed distance value from the boundary between muscle and subcutaneous fat at voxel p , which is extracted by thresholding (-70 [HU]), and a holes filling followed by morphological operation (opening and closing, radius = 5.0 [mm]) (Fig. 5c). The body mask extracted in the second step is used as the shape prior for $S_{p,q}$ because the shape is similar to the body cavity. In addition, we used low attenuation areas like air in lung as object seeds and bone regions as background seeds (see Fig. 5e and f). These regions are roughly extracted by a thresholding (-300 [HU] for low attenuation areas, 150 [HU] for bone). The value of λ and σ in $B_{p,q}$ (Boykov and Funka-Lea, 2006) of Eq. (12) is set to 0.1 and 10 and experimentally decided using a training dataset. Fig. 6 gives examples of segmentation results for cases with pathological abnormalities.

The registration process for the SSM of lungs and aorta uses landmarks placed on the body cavity label, as shown in Fig. 7c. First, we obtain the top and bottom slices of a rough segmentation of the lungs and find the four slices that are spatially uniformly distributed between the top and bottom slices, as shown in Fig. 7a,b. Landmarks are then automatically placed by finding the bounding boxes of the body cavity on the six slices and the topmost point of the spine in each slice. In order to register an SSM to an input image, we used the average position of the landmarks from the training data. We then performed a nonlinear transformation based on a biharmonic radial basis function (Feldmar et al., 1996; Fornefett et al., 1998). The rough segmentation results of

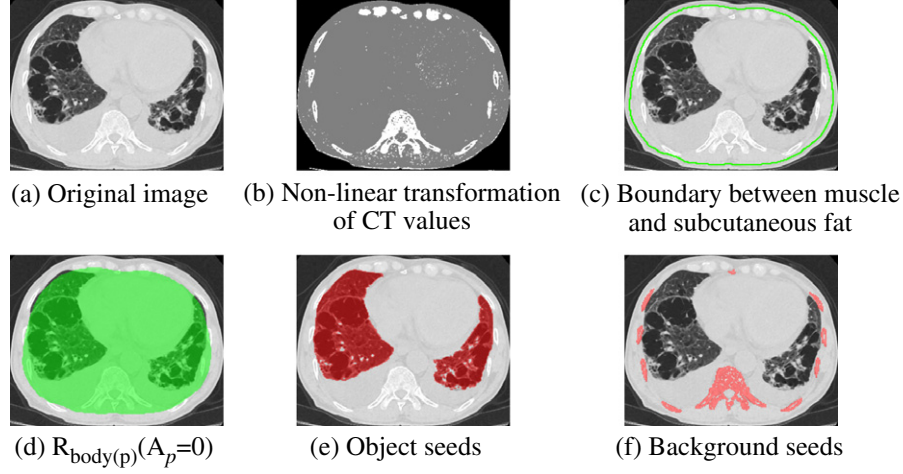


Fig. 5. Images for explanation of the body cavity segmentation procedure. (a) Original image, (b) Non-linear transformation of CT values, (c) Boundary between muscle and subcutaneous fat, (d) $R_{\text{body}(p)}(A_p=0)$, (e) Object seeds, and (f) Background seeds.

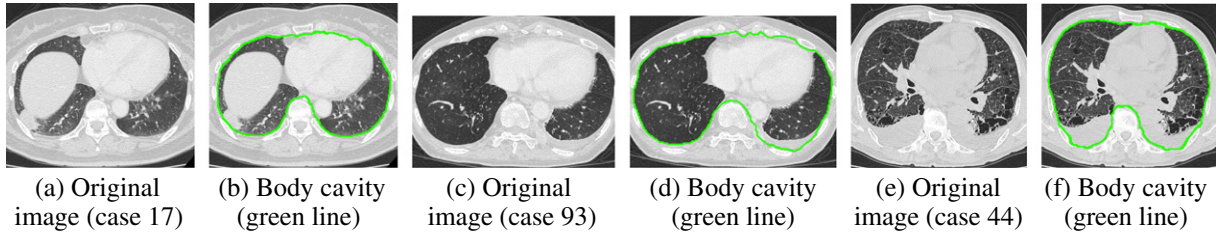


Fig. 6. Examples of segmentation results of a body cavity: (a) Original image (case 17), (b) Body cavity (green line), (c) Original image (case 93), (d) Body cavity (green line), (e) Original image (case 44), and (f) Body cavity (green line). (For interpretation of the references to color in this figure legend, the reader is referred to the web version of this article.)

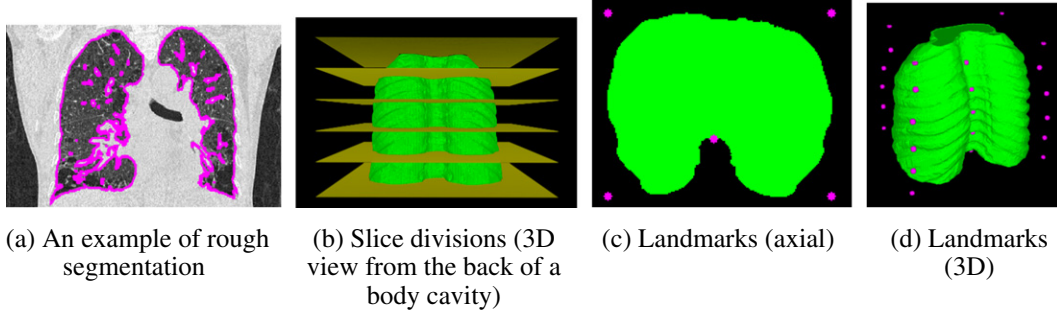


Fig. 7. An example of landmark placement using the result of rough lung segmentation and body cavity segmentation. (a) An example of rough segmentation. (b) Slice divisions (3D view from the back of a body cavity). (c) Landmarks (axial). (d) Landmarks (3D).

Fig. 7a might seem to be inaccurate. It is, however, accurate enough to place landmarks reliably. We would like to enhance that most of the segmentation error of the rough segmentation came from false negatives caused by vessels and lesions inside the lung which did not affect the decision of six slices of Fig. 7b as well as landmark placement of Fig. 7c and d.

The next process is aorta segmentation, which provides neighbor prior information, L_{nb} in Eq. (5), and uses a single-shape graph cut with the following energy function.

$$E(\mathbf{A}) = \lambda \cdot \sum_{p \in P} \{R_{\text{aorta}(p)}(A_p) + \text{Atlas}_p(A_p)\} + \sum_{\{p,q\} \in N} \{B_{p,q} + S_{p,q}\} \cdot \delta_{A_p \neq A_q} \quad (14)$$

$$R_{\text{aorta}(p)}(A_p) = \begin{cases} \Pr(\text{"other"} | \mathbf{F}_p) & (\text{if } A_p = 1) \\ \Pr(\text{"aorta"} | \mathbf{F}_p) & (\text{if } A_p = 0) \end{cases} \quad (15)$$

where \mathbf{F}_p represents a feature vector based on the intensity value at voxel p and $R_{\text{aorta}(p)}(A_p)$ is defined by posterior probabilities of aorta and other, both of which are computed from likelihood functions estimated by Parzen window estimator and uniform prior probabilities. $\text{Atlas}_p(A_p)$ is a prior probability of the aorta computed from training data. A registered shape template of an aorta from training data is used as the shape prior of $S_{p,q}$. We determined the value of λ and σ of Eq. (14) from the training data set. An example of a segmentation result is depicted in Fig. 8.

The next process is the estimation of patient-specific shapes. We calculated a Jaccard Index (JI) as a metric to compute the

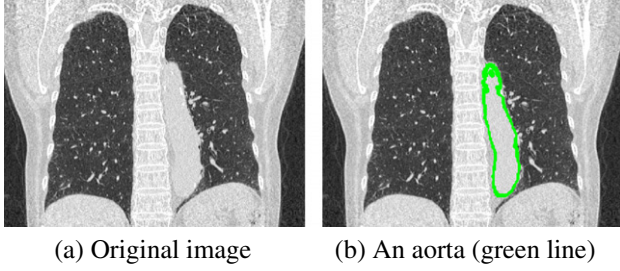


Fig. 8. An example of aorta segmentation results. (a) Original image. (b) An aorta (green line). (For interpretation of the references to color in this figure legend, the reader is referred to the web version of this article.)

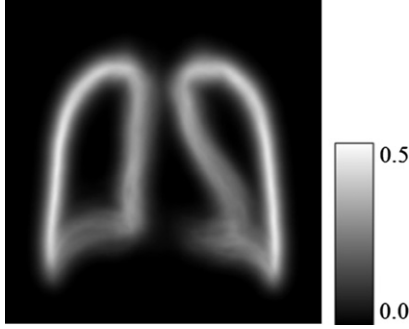


Fig. 9. Spatial weights used in WPCA.

distance between a rough segmented region and the shapes in an eigen shape space. Here, we employed a level set distribution model (LSDM) (Leventon et al., 2000) with a weighted principal component analysis (WPCA) (Skocaj et al., 2007) used as a statistical analysis method to construct the eigen shape space of a SSM, which has proved effective in modeling an organ's shape (Uchida et al., 2010). The spatial weights used in WPCA are depicted in Fig. 9. In this study, the rough segmentation result is projected to the eigen space spanned by the first two eigen modes and the closest shape to the rough segmentation is selected from among 25 shapes in the eigen shape space. In the multi-shape graph cuts, the top five closest shapes in terms of JI are chosen. The 25 shapes are generated by discretizing the eigen-shape space with 1σ spacing from the projection point with a range of $\pm 2\sigma$.

The final process is fine lung segmentation by the multi-shape graph cuts discussed in Section 2. In the next section, we will present several experimental results of a synthetic image and actual thoracic CT volumes, followed by discussion regarding the effectiveness of our proposed multi-shape graph cuts with neighbor constraints.

4. Experiments

4.1. Materials

4.1.1. Synthetic image

A 2D synthetic image (Shimizu et al., 2010) (Fig. 10c) was used to demonstrate the superiority of the multi-shape graph cuts over the single-shape graph cuts. In order to focus on the efficacy of $S_{p,q} \cdot \delta$ when using multiple shapes as opposed to a single shape, we minimized Eq. (16) below.

$$E(\mathbf{A}) = \lambda \cdot \sum_{p \in P} R_p(A_p) + \sum_{\{p,q\} \in N} \{B_{p,q} + S_{p,q}\} \cdot \delta_{A_p, A_q} < 0 \quad (16)$$

where we empirically determined the value of λ and σ in Eq. (16) to be 0.5 and 30, respectively. For the boundary term of the energy

function, we employed an eight-neighborhood system for this experiment.

The image includes not only an object (Fig. 10a), but also noise consisting of six structural noises (Fig. 10b) and an additive Gaussian noise ($N(0, 20^2)$) (Fig. 10c). The structural noises mimic lesions and vessels with different contrasts in an organ. The radius of the object in Fig. 10a is 40 [px] on average, and its amplitude, A , is 5 [px]. The distance dx and dy refer to the displacement of an object in the shape templates that were used as shape priors. In this experiment, we changed the amplitude A and distances dx and dy of the shape template to incorporate various deviations from the true shape. Uniform random numbers were used for the parameters A , dx , and dy (A : [5, 10], dx : $\{[-10, -5], [5, 10]\}$, dy : $\{[-10, -5], [5, 10]\}$); and generated 10 shape priors, an example of which is shown in Fig. 10d.

4.1.2. Clinical CT volumes

We performed lung segmentation using 97 cases with pulmonary diseases such as lung carcinoma, emphysema, and diffuse pulmonary disease. These cases included both non-contrast and contrast CT volumes scanned with breath holding (image size: $512 \times 512 \times 204\text{--}561$ [voxel], pixel size in an axial slice: 0.625–0.741 [mm/px], slice spacing: 0.5–1 [mm], bits stored: 16 [bit]). In this experiment, we included both a lung and a pleural cavity in the object targeted for segmentation and, for simplicity, denoted the area as lung in this section, as mentioned in our introduction. It is worth noting that all the processes are 3D automated. We employed a 26-neighborhood system for the graph cuts and divided the data into 40 (20: contrast, 20: non-contrast) training and 40 (20: contrast, 20: non-contrast) test datasets and 17 (8: contrast, 9: non-contrast) for training of hyper-parameters, such as graph cut parameters. The performance of the algorithm was then assessed by a cross validation test of two datasets of size 40. The training datasets of size 40 were used to build a probabilistic atlas, P_{atlas} and to calculate gray-value statistics in $R_p(A_p)$ of the lungs and other regions. The data were also used to construct a SSM of the lung in the patient-specific shape estimation process, and the shape template used in the aorta segmentation process. In addition, the gray-value statistics of the aorta for energy $R_{aorta(p)}(A_p)$ of Eq. (15) were computed from the corresponding training dataset in accordance with the DICOM tag of the contrast condition of an input CT volume, as the gray-value statistics of an aorta differs significantly between contrast and non-contrast CT volumes.

A training dataset of size 17 was used to decide λ and σ in Eq. (8). In the “Results” subsection below, the same parameter set is used for the comparison between the single-shape graph cuts and the multi-shape graph cuts. Actually, the λ and σ were fixed to 0.5 and 20 through all experiments, respectively, which was optimized for the single-shape graph cuts from the viewpoint of the performance index (PI) shown as Eq. (17) below.

$$PI = \frac{JI + S_{lesion}}{2.0} \quad (17)$$

where JI was computed between extracted lungs and true lungs approved by a medical doctor. S_{lesion} is the sensitivity of 60 lesions attached to the pleura of the chest wall, which are prone to being identified as background in lung segmentation. The above parameter set gave best performance on average for a training dataset of size 17 in the case of the single-shape graph cuts without neighbor constraints and adaptive weight but with Atlas.

4.2. Results

4.2.1. Synthetic Image

This experiment focused on the effectiveness of $S_{p,q} \cdot \delta$ when using multiple shapes. An example of the resultant images is

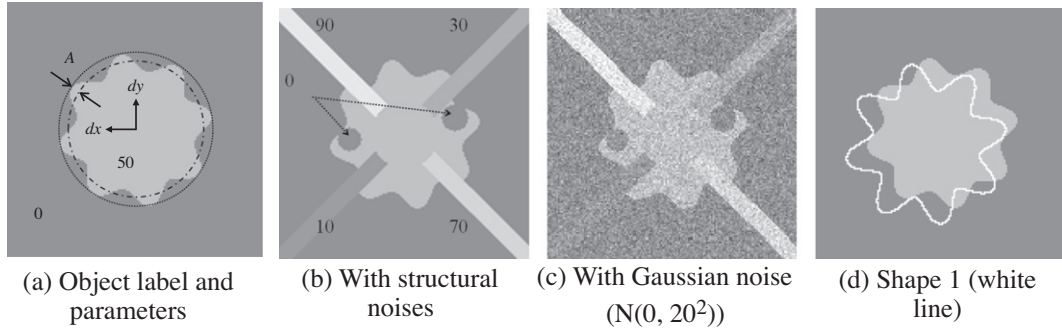


Fig. 10. Illustrations for a synthetic image (150×150). Numerals in (a) and (b) are the gray values of objects. (a) Object label and parameters. (b) With structural noises. (c) With Gaussian noise ($N(0, 20^2)$). (d) Shape 1 (white line).

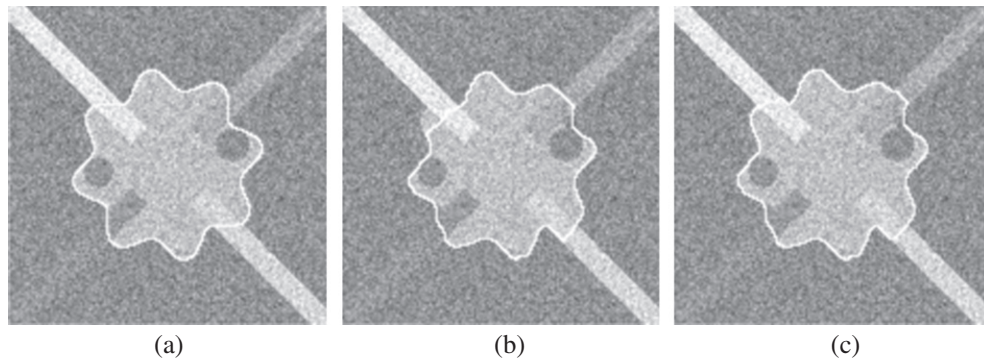


Fig. 11. Segmentation result of a synthetic image. (a) A true boundary (white line). (b) The result of single-shape graph cuts. (c) The result of multi-shape graph cuts.

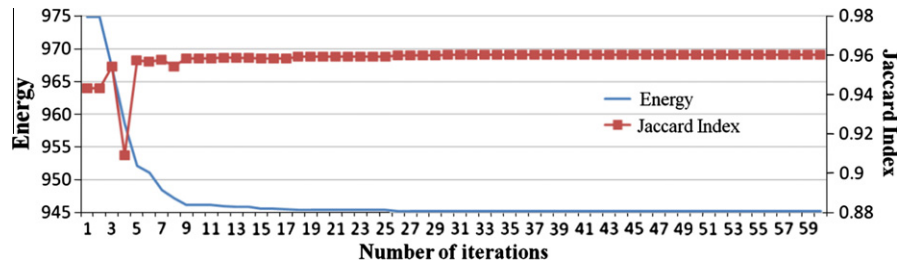


Fig. 12. Number of iterations vs. energy and segmentation performance.

shown in Fig. 11c. Fig. 12 displays the number of iterations, or proposals of labels, versus JI between the extracted regions and the true regions, and the number of iterations versus the total energy of the equation. Note that a different shape prior from Table 2 was proposed in every two iterations, or object and background proposals.

In Fig. 12, the total energy decreased monotonically, and the outline of JI tended to increase as the energy decreased. Specifically, JI increased from 0.943 to 0.960. The first JI shows the performance of single-shape graph cuts (Fig. 10b), while the last JI indicates that of the proposed multi-shape graph cuts (Fig. 11c). It was confirmed from these results that the multi-shape graph cuts could reduce segmentation errors by considering multiple shapes.

4.2.2. Clinical CT volumes

This experiment was designed to evaluate the difference in performance between the single-shape graph cuts and the multi-shape graph cuts, as well as the efficacy of the proposed neighbor constraints, or NB_p and $\delta_{NBp} = NBbq$, and adaptive weight $\lambda_{NB}(p)$. Con-

Table 2
Parameters of the shape priors.

Parameter	1	2	3	4	5	6	7	8	9	10
A	8	6	5	7	8	7	8	9	7	7
dx	9	8	-8	-7	-6	-10	-8	8	-7	9
dy	-7	8	8	-6	-8	-7	6	-7	-9	-9

sequently, experiments using all possible combinations of these constraints and the weight were conducted, and the JI of the 80 lungs and the sensitivity S_{lesion} of 60 lesions attached to the pleura of the chest wall, including pleural effusion were computed for the evaluation. In this experiment, we refer to the energy function without neighbor constraints and adaptive weight but with Atlas as the “conventional” energy function.

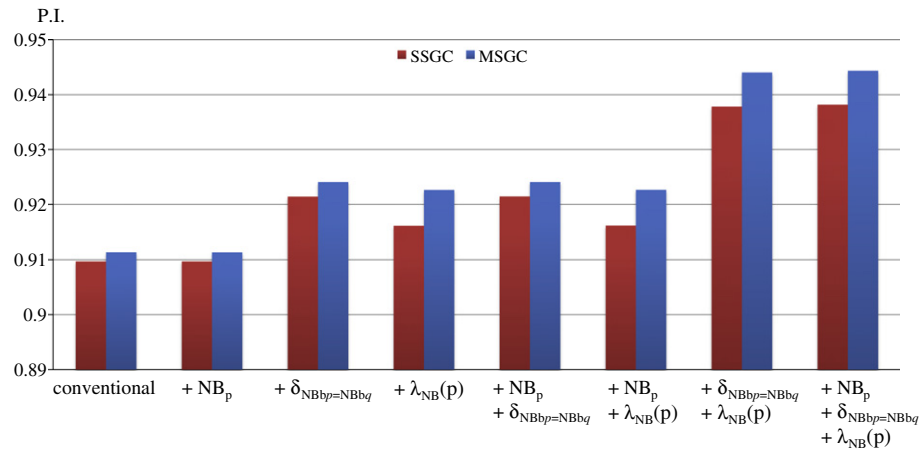
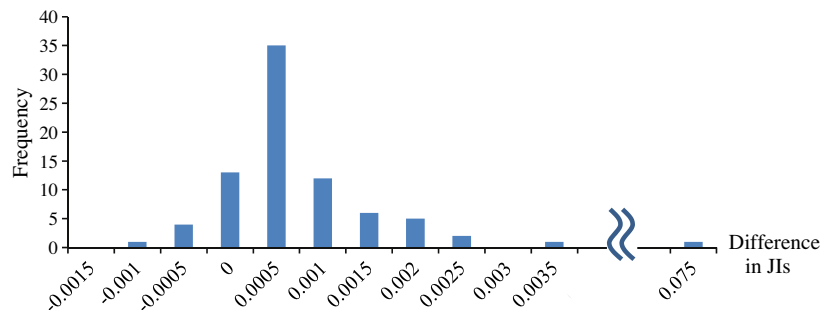
Table 3 presents the average and standard deviation of the JI, the sensitivity and PI, while Fig. 13 gives a bar graph of PI. The thresholding-based rough segmentation suffers from low accuracy (PI = 0.6027) due to false negatives of vessels and lesions in the

Table 3

The Jaccard Index of lungs and the sensitivity of lesions for graph cuts with different conditions. Note that abbreviations correspond to terms in the proposed energy of Eq. (8). “+” means addition of new terms to the conventional energy that is the energy function without neighbor constraints and adaptive weight but with Atlas.

		Jaccard Index		S_{lesion}		PI
		Average	STDV	Average	STDV	
SSGC	Rough segmentation	0.9558	0.0276	0.2495	0.1870	0.6027
	Conventional	0.9743	0.0237	0.8451	0.2592	0.9097
	+NB _p	0.9745	0.0236	0.8449	0.2591	0.9097
	+ $\delta_{\text{NBbp=NBbq}}$	0.9749	0.0198	0.8680	0.2221	0.9214
	+ $\lambda_{\text{NB}}(p)$	0.9735	0.0237	0.8588	0.2434	0.9162
	+NB _p + $\delta_{\text{NBbp=NBbq}}$	0.9752	0.0198	0.8677	0.2220	0.9215
	+NB _p + $\lambda_{\text{NB}}(p)$	0.9738	0.0236	0.8586	0.2433	0.9162
	+ $\delta_{\text{NBbp=NBbq}}$ + $\lambda_{\text{NB}}(p)$	0.9744	0.0144	0.9012	0.1477	0.9378
MSGC	+NB _p + $\delta_{\text{NBbp=NBbq}}$ + $\lambda_{\text{NB}}(p)$	0.9754	0.0135	0.9009	0.1476	0.9382
	Conventional	0.9756	0.0222	0.8471	0.2589	0.9114
	+NB _p	0.9758	0.0221	0.8468	0.2588	0.9113
	+ $\delta_{\text{NBbp=NBbq}}$	0.9761	0.0179	0.8720	0.2219	0.9241
	+ $\lambda_{\text{NB}}(p)$	0.9751	0.0222	0.8702	0.2337	0.9226
	+NB _p + $\delta_{\text{NBbp=NBbq}}$	0.9764	0.0178	0.8718	0.2218	0.9241
	+NB _p + $\lambda_{\text{NB}}(p)$	0.9753	0.0221	0.8700	0.2336	0.9227
	+ $\delta_{\text{NBbp=NBbq}}$ + $\lambda_{\text{NB}}(p)$	0.9759	0.0115	0.9122	0.1328	0.9440
	+NB _p + $\delta_{\text{NBbp=NBbq}}$ + $\lambda_{\text{NB}}(p)$	0.9768	0.0105	0.9119	0.1327	0.9443

NB_p: data term for neighbor constraint, $\delta_{\text{NBbp=NBbq}}$: boundary term for neighbor constraint, $\lambda_{\text{NB}}(p)$: adaptive weight.

**Fig. 13.** PI for graph cuts with different conditions.**Fig. 14.** A histogram of difference between JI of the multi-shape graph cuts and that of the single-shape graph cuts (= JI of the multi-shape graph cuts – JI of the single-shape graph cuts) with all neighbor constraints and adaptive weight.

lung. The single-shape graph cuts with the conventional energy function significantly increased the PI from 0.6027 to 0.9097. In particular, the sensitivity was improved from 0.2495 to 0.8451 because the shape-based graph cuts worked quite well for lesions attached to the pleura of the chest walls. We added the proposed neighbor constraints and the adaptive weight one by one and tested all possible combinations. In general, the more the neighbor constraints were added, the better the PI became. In addition, the adaptive weight improved the performance. The best performance

of the single-shape graph cuts was achieved by the graph cuts with all neighbor constraints and the adaptive weight whose PI was 0.9382.

The lower half of the table shows the results of the multi-shape graph cuts. By comparing each result to the single-shape graph cuts with same constraints, we found that multiple shapes always boosted the performance of segmentation from the viewpoint of not only the Jaccard Index but also the sensitivity. Consequently, the best performance among all methods was achieved by the

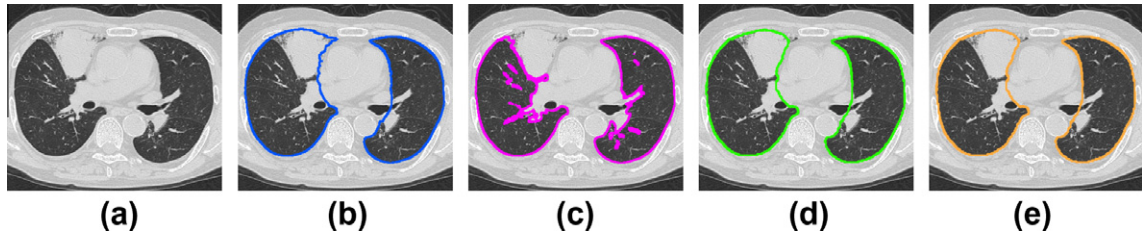


Fig. 15. Examples of segmentation results: (a) original image, (b) true boundaries, (c) rough segmentation, (d) single-shape graph cuts (conventional), and (e) multi-shape graph cuts (Eq. (8)).

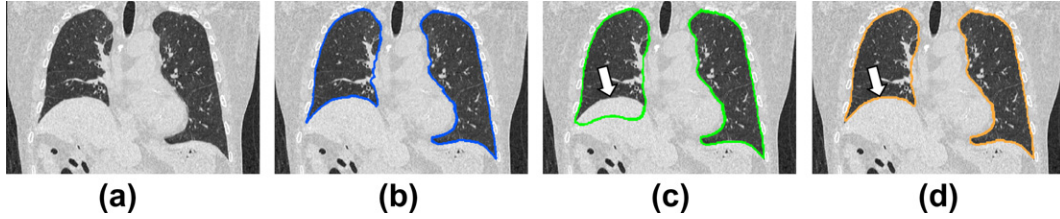


Fig. 16. Examples of segmentation results: (a) original image, (b) true boundaries, (c) single-shape graph cuts, and (d) multi-shape graph cuts.

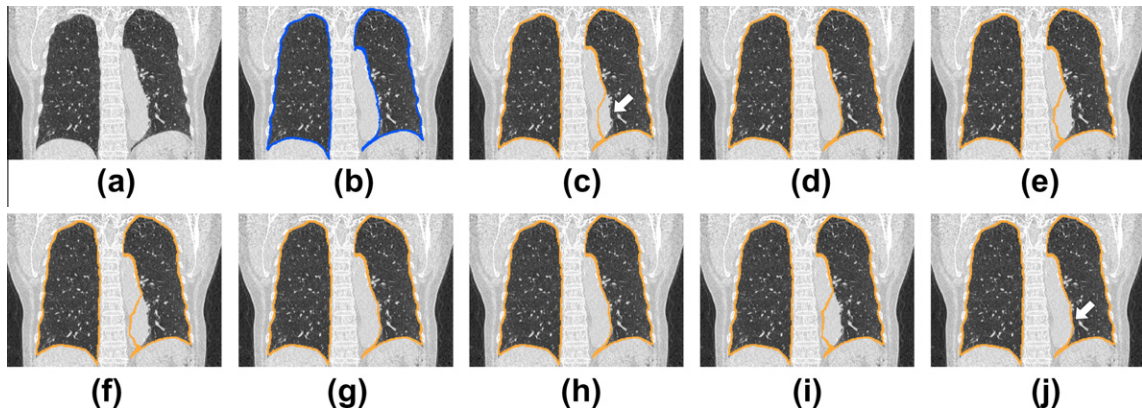


Fig. 17. Examples of lung segmentation results for the case in which the shape of the aorta deviates from that of the normal population: (a) original image, (b) true boundaries, (c) conventional, (d) $+NB_p$, (e) $+δNB_{bp}=NB_{bq}$, (f) $+λ_{NB}(p)$, (g) $+NB_p + δNB_{bp}=NB_{bq}$, (h) $+NB_p + λ_{NB}(p)$, (i) $+δNB_{bp}=NB_{bq} + λ_{NB}(p)$, and (j) $+NB_p + δNB_{bp}=NB_{bq} + λ_{NB}(p)$.

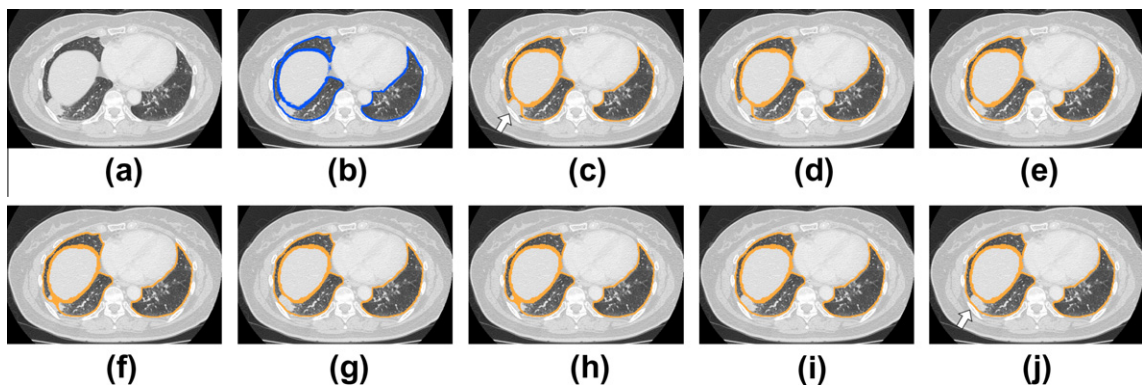


Fig. 18. Examples of lung segmentation results for the case in which a pathological abnormality is attached to the pleura of the chest wall: (a) original image, (b) true boundaries, (c) conventional, (d) $+NB_p$, (e) $+δNB_{bp}=NB_{bq}$, (f) $+λ_{NB}(p)$, (g) $+NB_p + δNB_{bp}=NB_{bq}$, (h) $+NB_p + λ_{NB}(p)$, (i) $+δNB_{bp}=NB_{bq} + λ_{NB}(p)$, and (j) $+NB_p + δNB_{bp}=NB_{bq} + λ_{NB}(p)$.

multi-shape graph cuts with all neighbor constraints and the adaptive weight whose PI was 0.9443.

In spite of the improvement in performance by the proposed method, the differences, in particular difference in JI between

methods are small, sometimes below 0.01. This is due to that fact that lung is an organ with very large volume and the JI in our study is close to 1, an improvement in a local area does not change the JI too much. Figs. 17c, j and 19c, j in the next section

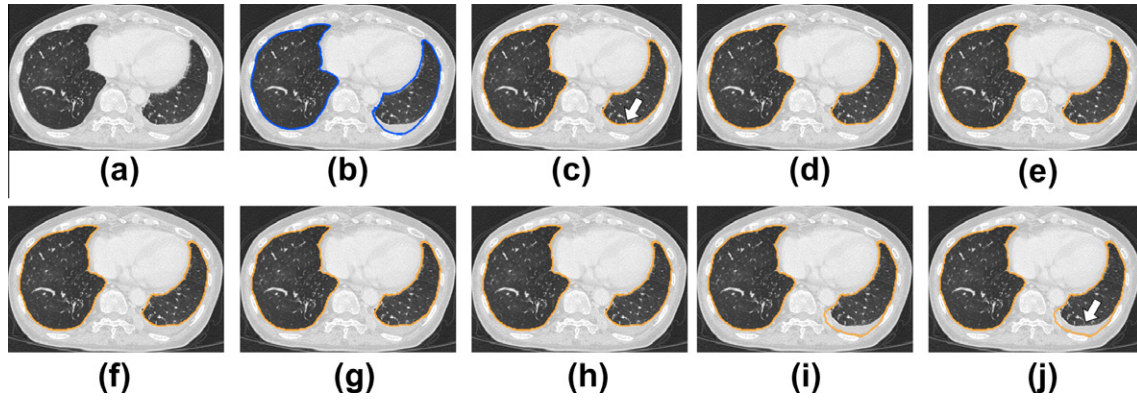


Fig. 19. Examples of lung segmentation results for a case of pleural effusion: (a) original image, (b) true boundaries, (c) conventional, (d) $+NB_p$, (e) $+ \delta_{NBbp=NBbq}$, (f) $+ \lambda_{NB}(p)$, (g) $+NB_p + \delta_{NBbp=NBbq}$, (h) $+NB_p + \lambda_{NB}(p)$, (i) $+ \delta_{NBbp=NBbq} + \lambda_{NB}(p)$, and (j) $+NB_p + \delta_{NBbp=NBbq} + \lambda_{NB}(p)$.

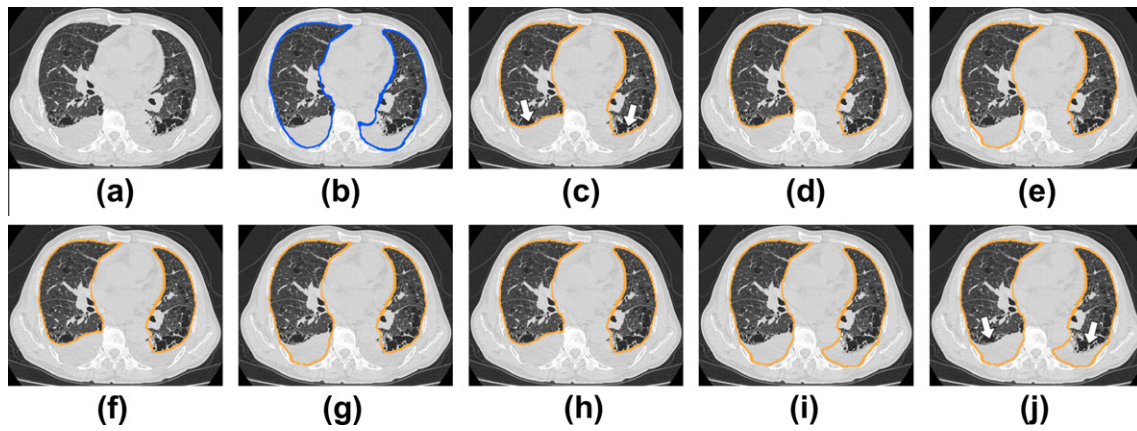


Fig. 20. Examples of lung segmentation results for a case of pleural effusion: (a) original image, (b) true boundaries, (c) conventional, (d) $+NB_p$, (e) $+ \delta_{NBbp=NBbq}$, (f) $+ \lambda_{NB}(p)$, (g) $+NB_p + \delta_{NBbp=NBbq}$, (h) $+NB_p + \lambda_{NB}(p)$, (i) $+ \delta_{NBbp=NBbq} + \lambda_{NB}(p)$, and (j) $+NB_p + \delta_{NBbp=NBbq} + \lambda_{NB}(p)$.

are good examples where differences in JI (0.0060(=Fig. 17j–c), 0.0028(=Fig. 19j–c)) are small but the improvements should be meaningful from the view point of a subsequent analysis for computer-aided diagnosis of lung. In addition, we carried out statistical tests to evaluate the statistical difference in performance between the graph cuts with different conditions using the Wilcoxon signed-rank test (H_0 : there is no significant difference in performance between the two graph cuts). Fig. 14 is an example of histogram of the difference between JI of the multi-shape graph cuts and that of the single-shape graph cuts (= JI of the multi-shape graph cuts – JI of the single-shape graph cuts) with all neighbor constraints and adaptive weight. This figure suggests the superiority of the multi-shape graph cuts, because most of the differences have positive signs. All results of the Wilcoxon test for the JI of the lungs and the sensitivity of lesions are summarized in the Tables in Appendix B. From the Tables, it was confirmed that 88.3 [%] of all pairs of two methods has statistically significant difference in JI, and the difference in sensitivity S_{lesion} of 48.3 [%] of all pairs was statistically significant. The difference in JI between the single-shape and the multi-shape graph cuts was confirmed to be significant with a risk of $p < 0.01$ when two methods employed the same energy function (see the pairs of underlined asterisks in the Appendix Table B.1). In contrast, the difference in the sensitivity was not statistically significant ($p > 0.05$). This fact indicates that the multiple-shapes based method is effective in boosting the performance of whole lung segmentation but not that of the sensitivity. The sensitivity S_{lesion} was, however, improved when either of $\delta_{NBbp=NBbq}$ and adaptive weight $\lambda_{NB}(p)$

was added to the energy function of the multi-shape graph cuts (see the pairs of underlined asterisks in the Appendix Table B.2).

It is worth mentioning that it is impossible to carry out a statistical test of PI which is an average of JI of 80 cases and sensitivity of 60 lesions. It is a single value computed from all cases. If each case has lesions, we can define a P.I. of each case and perform a statistical test. Some cases, however, do not have any pathological lesion in the CT volumes. Consequently we carried out statistical tests of JI and sensitivity, individually.

Fig. 15a–e illustrate a case of pathological abnormality attached to the pleura of the chest wall in which shape prior based methods, or both the single shape and the multi-shape graph cuts were superior to the thresholding based rough segmentation. The JI of this case was improved from 0.9332 (Fig. 15c) to 0.9752 (Fig. 15e), and the sensitivity was improved from 0.1421 to 0.9519.

Fig. 16a–d illustrate a case in which the single-shape graph cuts overextracted liver region, while the multi-shape graph cuts did not. The JI in this case was improved from 0.8993 to 0.9733 when multi-shape graph cuts were used.

Figs. 17–20 depict examples of segmentation results for multi-shape graph cuts that demonstrate the effectiveness of the neighbor constraints. Fig. 17 is a case in which the results of the graph cuts with the NB_p regarding aorta (Fig. 17d, g, h, and j) were superior to those without the NB_p (Fig. 17e, f, and i). For example, the JI of Fig. 17c, 0.9737, was improved to 0.9797 (Fig. 17j), due to the reduction of the false positive of the aorta region. Fig. 18 shows that the graph cuts with $\delta_{NBbp=NBbq}$ (Fig. 18e, g, i, and j) achieved better segmentation than those without $\delta_{NBbp=NBbq}$ (Fig. 18d, f,

and h), in terms of the sensitivity of the lesion in particular. The sensitivity of the lesion was improved from 0.5861 (Fig. 18c) to 0.9638 (Fig. 18j). Finally, Figs. 19 and 20 show the effectiveness of the combination of $\lambda_{NB}(p)$ and $\delta_{NBb|p=NBbq}$ in cases with pleural effusion. The sensitivity of the pleural effusion was significantly improved from 0.0146 (Fig. 19c) to 0.9126 (Fig. 19j), and from 0.0292 (Fig. 20c) to 0.6757 (Fig. 20j). Further discussion will be given in the next section.

5. Discussion

5.1. Synthetic Image

Fig. 21 shows the segmentation results for the fourth and fifth iterations along with their shape priors. Here, the performance changed rapidly between the iterations, as can be seen in Figs. 12 and 21. The fourth iteration (“background” proposal of the second shape prior) generated significant false negatives, as indicated by the arrow, as a result of the improper shape of (a). The result was a rapid decrease in the JI, as graphically illustrated in Fig. 12. However, when the third shape prior of (c), which is more similar to the true shape in terms of gradient vectors distribution, was proposed, the multi-shape graph cuts succeeded in extracting the region. The remaining iterations kept the shape of (d). The false negatives of (b) never recurred because the energy of (d) was smaller than that of (b). From the above, we concluded that if an appropriate shape prior similar to the true shape is included in a set of proposed shapes, the multi-shape graph cuts can combine the shapes appropriately, as shown in Fig. 22, resulting in higher accuracy in segmentation than the single-shape graph cuts.

5.2. Clinical CT volumes

As presented in the results of clinical CT volumes in Section 4, the multi-shape graph cuts were superior to the single-shape graph cuts, while maintaining high sensitivity to lesions. Although even a single shape prior in segmentation of the lungs with lesions is advantageous, as shown in Fig. 15, there are limitations on the single-shape graph cuts, as observed in Fig. 16c. Fig. 23 presents shape priors used for the case of Fig. 15, where the top five shape priors with the highest similarity to rough segmentation are displayed. The major reason for the success of the single-shape graph cuts in Fig. 15 is the fact that the first estimated shape, or a shape prior used in the single shape graph cuts, was quite similar to the true shape. In contrast, the case in Fig. 16c ended up being an inaccurate segmentation as the first estimated shape was far from the true shape, as shown in Fig. 24. However, the second shape prior of Fig. 24b, which is similar to the true shape, boosted the segmentation performance when it was used in the multi-shape graph cuts presented in Fig. 16d. It should be noted that the segmentation re-

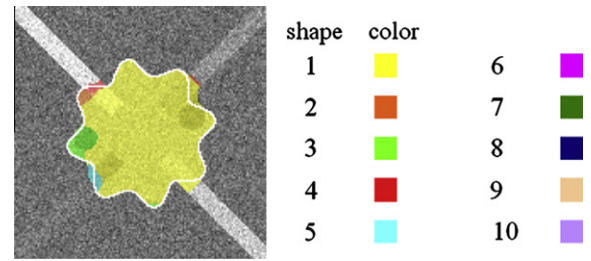


Fig. 22. Final segmentation result with its corresponding label in color. (For interpretation of the references to color in this figure legend, the reader is referred to the web version of this article.)

sults never return to the inaccurate results derived from the first shape prior because the segmentation results with the second shape prior achieved smaller energy than that of the first shape prior. This is consistent with the above discussion of the synthetic image-based experiment. The multi-shape graph cuts can effectively utilize shape information among multiple shape priors, resulting in it being superior to the single-shape graph cuts.

Fig. 25 is the worst case in Fig. 14 where JI of the multi-shape graph cuts was decreased by 0.0012 comparing to the single-shape graph cuts. Major difference in segmentation between the two graph cuts exists in hilum of lung. The distance between the two extracted surfaces in hilum is small but the extent of the difference is large, resulting in maximum decreasing in JI. In contrast, no change in sensitivity was observed, because this case does not have any lesion in hilum of lung.

One of the important parameters in the proposed multi-shape graph cuts is the number of shape priors. To determine this parameter, we paid attention to the following two facts: Once a shape prior gives good estimation of the shape, the multi-shape graph cuts achieves the best performance and never returns to the worse segmentation result with high energy. In addition, the computation cost is proportional to the number of shape priors. Consequently, we empirically set the number to 5 (= n in Section 2) which means 10 iterations of object or background proposal, because each shape prior corresponds to a pair of object and background proposals. The optimization of the number of shape priors remains important future work to be carried out by us.

In the following paragraph, we will discuss the effectiveness of the proposed neighbor constraints in overcoming the limitations of the shape-based graph cuts with a conventional energy function. Fig. 26 presents the shape priors of Fig. 17a–j. Since the shape of the aorta region of this case is unique and differs from those in the training dataset, it was impossible to estimate the shape of the lungs correctly. Consequently, there was no shape among the estimated shapes that resembled the aorta. The failure of the conventional energy function (Fig. 17c) could be explained by the

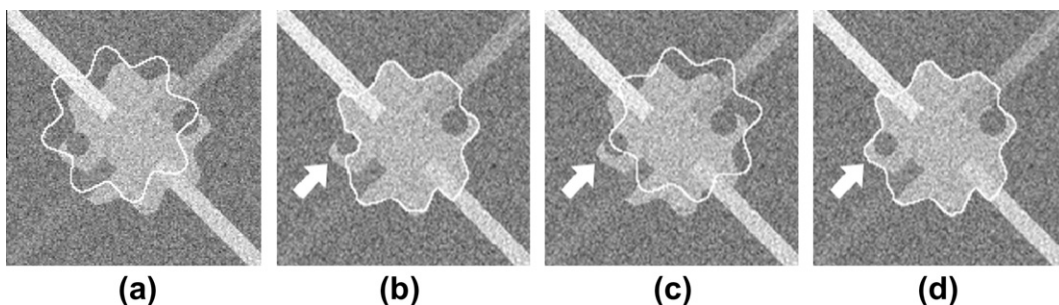


Fig. 21. The shape prior and the segmentation results of the fourth and fifth iterations: (a) the shape prior of the fourth iteration (“background” proposal), (b) the result of the fourth iteration, (c) the shape prior of the fifth iteration (“object” proposal), and (d) the result of the fifth iteration.

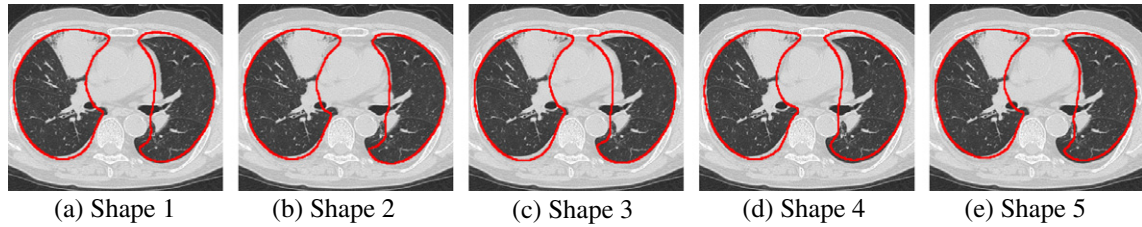


Fig. 23. Shape priors used for the case in Fig. 15. (a) Shape 1, (b) Shape 2, (c) Shape 3, (d) Shape 4, and (e) Shape 5.

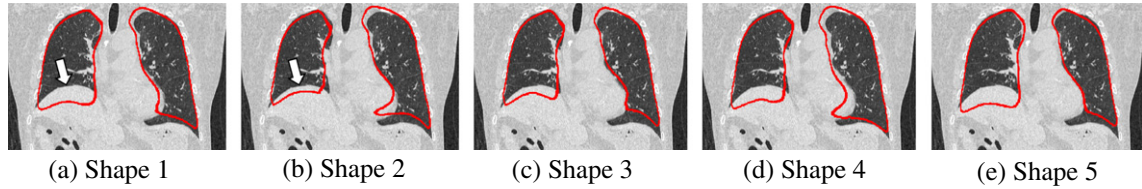


Fig. 24. Shape priors used for the case in Fig. 16. (a) Shape 1, (b) Shape 2, (c) Shape 3, (d) Shape 4, and (e) Shape 5.

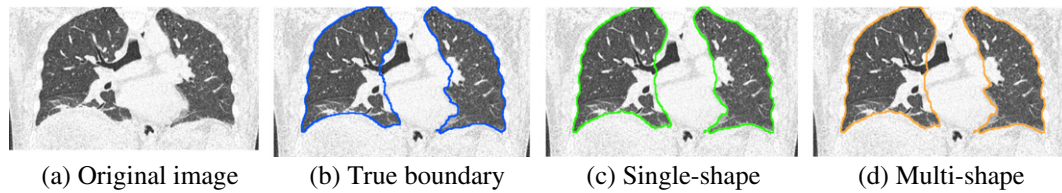


Fig. 25. The worst case in Fig. 14 where JI of the multi-shape graph cuts was decreased by 0.0012 comparing to the single-shape graph cuts. (a) Original image. (b) True boundary. (c) Single-shape. (d) Multi-shape.

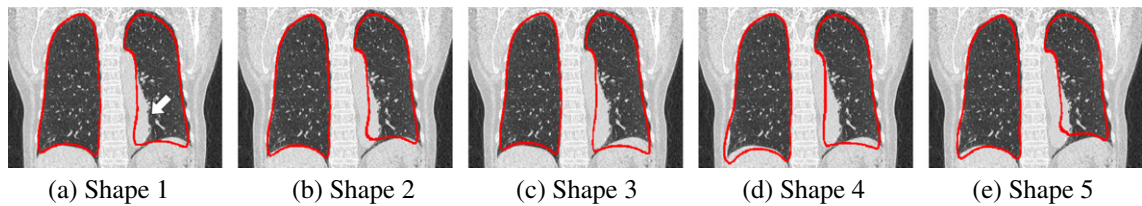


Fig. 26. Shape priors used for the case in Fig. 17. (a) Shape 1, (b) Shape 2, (c) Shape 3, (d) Shape 4, and (e) Shape 5.

above reasons, and this is a limitation of the shape-based graph cuts using the conventional energy function. However, this limitation can be overcome by the proposed neighbor constraint, NB_p . Figs. 17d, g, h, and j are good examples that demonstrate that the graph cuts with NB_p are able to reduce the false positives of an aorta region as the aorta region was successfully segmented, as seen in Fig. 8b.

It is worth discussing the possible limitations of such neighbor constraints, which might be caused by segmentation error of the neighbor structures. Actually, there were small errors in segmentation of the aorta region, resulting in a slight decrease in the sensitivity of the lesions. Therefore, we can state that as far as the segmentation result of the neighbor regions is reliable, such neighbor constraint will boost the performance of the segmentation. In our study, the advantage of the NB_p was larger than the aforementioned disadvantage.

Our next discussion will now focus on the combination of the neighbor constraint $\delta_{NBp=NBq}$ and adaptive weight $\lambda_{NB}(p)$. Table 3,

along with Figs. 13 and 18–20 indicate the effectiveness of the constraint and the weight, especially for the case in which pathological abnormalities are attached to the pleura of the chest walls. This is due to the fact that the extracted body cavity provides fairly accurate information regarding the lung boundary, except for the boundary near the mediastinum (see Fig. 6). The body cavity extraction process focuses on bones that are easy to extract, leading to it being robust against pathologies. Moreover, the adaptive weight put larger weight to the reliable boundary. As a result, the combination was effective in determining the boundary between pathologies both in the lungs and outside the regions of the lungs. However, we should also note that the performance of the proposed graph cuts depends on the segmentation accuracy of the body cavity—in particular, false negative of lung, which might cause false negative of lung lesions. We evaluated the size of the overlooked regions in the body cavity extraction process and found that the average rate of false negatives, normalized by volume of lung region, was 0.562 ± 0.207 [%], which was quite

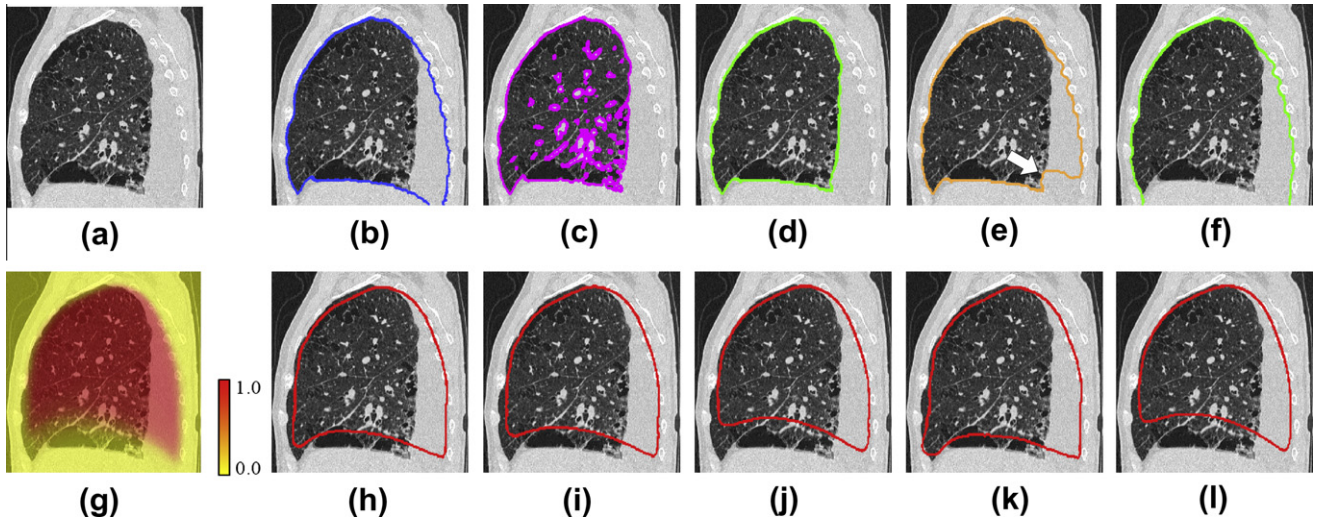


Fig. 27. The case of pleural effusion: (a) Original image, (b) true boundaries, (c) rough segmentation, (d) conventional, (e) proposed, (f) body cavity segmentation, (g) prior probability (h) Shape 1, (i) Shape 2, (j) Shape 3, (k) Shape 4, and (l) Shape 5.

low. Most of the false negative regions were located in healthy lung and only 2.552 [%] occurred in the lesions, resulting in only a small effect on S_{lesion} .

We now discuss the case of pleural effusion depicted in Fig. 20. Fig. 27 presents the detailed experimental results for this case. The rough segmentation based only on appearance failed to extract the pleural effusion (see Fig. 27c). Fig. 27h–l show the estimated shapes that provide fairly useful information about the shape near the dorsal ribs. The multi-shape graph cuts with the conventional energy function, however, failed to extract the region near the dorsal ribs as presented in Fig. 27d. Because the contrast between air in lung and pleural effusion was very high, the boundary term, B_{pq} , derived the boundary of the two regions to be the final boundary of the segmentation. In this case, the neighbor constraint $\delta_{NBbp=NBbq}$ played an important role in the segmentation by the graph cuts. As in Fig. 27f, the body cavity was successfully extracted and it led to successful segmentation of the lung by the graph cuts with $\delta_{NBbp=NBbq}$ and adaptive weight $\lambda_{NB}(p)$.

One of the limitations of the proposed lung segmentation system exists in the low accuracy in segmentation of the bottom part of the lungs with pleural effusion. The case of Figs. 20 and 27 is a typical example. Although the sensitivity was increased from 0.0292 (Figs. 20c and 27d) to 0.6757 (Figs. 20j and 27e) by the neighbor constraints with adaptive weight, the bottom part of the pleural effusion were overlooked during the segmentation process (see Fig. 27e). This failure is attributable to the low prior probability given by the $Atlas_p(A_p)$ and the low shape estimation accuracy (see Fig. 27g–l). In order to boost the segmentation accuracy, further improvement of the Atlas, as well as the shape estimation process, remains as important future work.

Finally, the computation time of our algorithm was approximately 15–30 min per CT volume (Intel(R) Core(TM) i7 3.07 GHz \times 2). This time varied on a case-by-case basis, depending on the number of iterations of fusion move, the average number of iterations of the fusion move operator in algorithm 1 was 54.

Our future plans are as follows. First we plan to optimize the number of shape priors used in the multi-shape graph cuts. Further experiments with more cases of severe pathologies in the lung fields are also important work, which should be followed by improvements of the registration process for SSM of lungs and aorta by, for example, employing a simultaneous registra-

tion–segmentation scheme, and improvements of the shape energy, including proposal of a new shape energy that addresses shrinking bias problem (Vicente et al., 2008; Hanaoka et al., 2011). Comparison in performance of plural effusion extraction with other methods, such as registration based methods proposed by Sluimer et al. (2008) and Kido and Tsunomori (2009) is another interesting future work. Finally we plan to apply the proposed multi-shape graph cuts with neighbor constraints to another segmentation problem, such as multi-organ segmentation from medical imagery.

6. Conclusion

This paper proposed a novel graph cut algorithm that can take into account multiple-shapes and neighbor structure constraints, and applied this algorithm to lung segmentation from a chest CT volume. The contributions of this paper are as follows:

- (1) Proposal of a graph cut-based segmentation algorithm that can take into account the multiple possible shapes of a target object. The salient feature of the algorithm is that it can automatically choose an optimal shape prior from among multiple priors at each voxel by minimizing the proposed sub-modular energy function. The minimization is performed in a sequential manner by the fusion move algorithm that uses the QPBO min-cut algorithm.
- (2) Proposal of novel energy terms so as to introduce prior knowledge on neighboring structures of a target into the graph cut algorithm.
- (3) To validate the performance of the proposed method, experiments using a synthetic image and 97 clinical CT volumes were conducted. The experiment that utilized the synthetic image demonstrated the superiority of multiple shapes over a single shape. The results of lung segmentation from clinical CT volumes are summarized as follows:
 - (a) Multi-shape graph cuts were proven to be more beneficial than single-shape graph cuts. The Jaccard Index between an extracted region and a true region was enhanced by the multi-shape graph cuts with statistical difference from the single-shape graph cuts ($p < 0.01$, Wilcoxon test) while keeping the sensitivity of the lesion at the same level.

- (b) The neighbor constraints by the aorta and the body cavity played an important role in the lung segmentation process—especially when extracting lungs that have unique shapes and lungs with pathological abnormalities including pleural effusion—resulting in improvement in the sensitivity of the lesions.
- (c) Among the methods tested in this paper, the multi-shape graph cuts with all neighbor constraints and adaptive weight achieved the best performance from the point of view of the Jaccard Index of lung (0.9768 ± 0.0105) and sensitivity of lesions (0.9119 ± 0.1327).

Appendix A. Proof of the sub-modularity of the proposed energy term

Here we give an intuitive proof of inequality (A.1) below (Lempitsky et al., 2010) to show the sub-modularity of the proposed energy term:

$$f_{pq}(X_p^{\text{cur}}, X_q^{\text{cur}}) + f_{pq}(X_p^{\text{pro}}, X_q^{\text{pro}}) \leq f_{pq}(X_p^{\text{cur}}, X_q^{\text{pro}}) + f_{pq}(X_p^{\text{pro}}, X_q^{\text{cur}}) \quad (\text{A.1})$$

where X_p^{cur} is a current label, X_p^{pro} is a proposed label at voxel p , and f_{pq} means $S_{p,q} \cdot \delta$.

Proof. There are three cases with different signs of the product of $X_p^{\text{cur}}, X_q^{\text{cur}}$ and the proposal label $l \in L$, in which the three cases are mutually exclusive events and together cover all possible events. Note that the product of two labels is positive if the labels belong to the same class, but negative otherwise.

- Case 1: $X_p^{\text{cur}} X_q^{\text{cur}} > 0$

$f_{pq}(X_p^{\text{cur}}, X_q^{\text{cur}}) = f_{pq}(X_p^{\text{pro}}, X_q^{\text{pro}}) = 0$, because of the function δ . Therefore, we can write Eqs. (A.1) as (A.2), as follows:

$$0 + 0 \leq f_{pq}(X_p^{\text{cur}}, X_q^{\text{pro}}) + f_{pq}(X_p^{\text{pro}}, X_q^{\text{cur}}) \quad (\text{A.2})$$

Since f_{pq} is greater than or equal to 0, the above inequality is always met.

Table B.1

Wilcoxon signed-rank test for the Jaccard Index between results of different methods. (A: conventional, B: +NB_p, C: + $\delta_{\text{NBbp=NBbq}}$, D: + λ_{NB} , E: +NB_p + $\delta_{\text{NBbp=NBbq}}$, F: +NB_p + $\lambda_{\text{NB}}(p)$, G: + $\delta_{\text{NBbp=NBbq}}$ + $\lambda_{\text{NB}}(p)$, H: +NB_p + $\delta_{\text{NBbp=NBbq}}$ + $\lambda_{\text{NB}}(p)$ (energy of Eq. (8)), S: single-shape graph cuts, M: multi-shape graph cuts).

		A		B		C		D		E		F		G		H	
		S	M	S	M	S	M	S	M	S	M	S	M	S	M	S	M
A	S		**	**	**	**	**	**	**	**	**	**	**	**	**	**	**
	M		—	**	**	**	**	**	**	*	**	**	**	**	**	**	**
B	S				**		*	**	**		**	**	*	**	**	**	*
	M				—	**	**	**	**	**	*	**	**	**	**	**	**
C	S						**	**		**	**	**		**	**	**	*
	M						—	**	**	**	**	**	**	**	**	**	**
D	S							**		**	**	**	**		**	**	**
	M						—	**		**	**	**	**	**	**	**	**
E	S									**	**		**	**	**	**	**
	M									—	**	**	**	**	**	**	**
F	S											**	**	*		**	**
	M										—	**	**	**	**	**	**
G	S													—	**	**	**
	M														—	**	**
H	S																—
	M																—

Table B.2

Wilcoxon signed-rank test for the S_{lesion} between results of different methods. (A: conventional, B: +NB_p, C: + $\delta_{\text{NBbp=NBbq}}$, D: + λ_{NB} , E: +NB_p + $\delta_{\text{NBbp=NBbq}}$, F: +NB_p + $\lambda_{\text{NB}}(p)$, G: + $\delta_{\text{NBbp=NBbq}}$ + $\lambda_{\text{NB}}(p)$, H: +NB_p + $\delta_{\text{NBbp=NBbq}}$ + $\lambda_{\text{NB}}(p)$ (energy of Eq. (8)), S: single-shape graph cuts, M: multi-shape graph cuts).

		A		B		C		D		E		F		G		H	
		S	M	S	M	S	M	S	M	S	M	S	M	S	M	S	M
A	S					*		**	*			**	*	**	**	**	**
	M					**	*	**		*	*	**	*	**	**	**	**
B	S					*	*	**	*	*	*	**	*	**	**	**	**
	M					*	**	*	**	**	*	**	*	**	**	**	**
C	S													**	*	**	*
	M													*	**	*	**
D	S																
	M																
E	S													**	**	**	*
	M													*	**	*	**
F	S																
	M														*		
G	S																
	M																
H	S																
	M																

- Case 2: $X_p^{\text{cur}} X_q^{\text{cur}} < 0$ and $X_p^{\text{cur}} l > 0$

Since X_p^{cur} belongs to the same class as proposal label l , $X_p^{\text{pro}} \leftarrow X_p^{\text{cur}}$. Since X_q^{cur} belongs to a different class from proposal label l , $X_q^{\text{pro}} \leftarrow l$. Therefore, we can write Eqs. (A.1) as (A.3), which is an algebraic identity.

$$f_{pq}(X_p^{\text{cur}}, X_q^{\text{cur}}) + f_{pq}(X_p^{\text{cur}}, l) = f_{pq}(X_p^{\text{cur}}, l) + f_{pq}(X_p^{\text{cur}}, X_q^{\text{cur}}) \quad (\text{A.3})$$

- Case 3: $X_p^{\text{cur}} X_q^{\text{cur}} < 0$ and $X_p^{\text{cur}} l < 0$.

Since X_p^{cur} belongs to a different class from proposal label l , $X_p^{\text{pro}} \leftarrow l$. Since X_q^{cur} belongs to the same class as proposal label l , $X_q^{\text{pro}} \leftarrow X_q^{\text{cur}}$. Therefore, we can write Eqs. (A.1) as (A.4), which is also an algebraic identity.

$$f_{pq}(X_p^{\text{cur}}, X_q^{\text{cur}}) + f_{pq}(l, X_q^{\text{cur}}) = f_{pq}(X_p^{\text{cur}}, X_q^{\text{cur}}) + f_{pq}(l, X_q^{\text{cur}}) \quad (\text{A.4})$$

□

Appendix B. Wilcoxon signed-rank test between all combinations of energy functions

Tables B.1 and B.2 presents all the results of the Wilcoxon signed-rank test (H_0 : there is no significant difference between the two performances) for the Jaccard Index of the lungs and the sensitivity of lesions. The symbols “*” and “**” indicate that the difference between the two performances is statistically significant with a risk of $p < 0.01$ and $p < 0.05$, respectively. The meaning of the underline was explained in Section 4.2.

References

- Boykov, Y., Veksler, O., Zabih, R., 2001. Fast approximate energy minimization via graph cuts. *IEEE Transactions on Pattern Analysis and Machine Intelligence* 23 (11), 1222–1239.
- Boykov, Y., Funka-Lea, G., 2006. Graph cuts and efficient N-D image segmentation. *International Journal of Computer Vision* 70 (2), 109–131.
- Cremers, D., Rousson, M., Deriche, R., 2007. A review of statistical approaches to level set segmentation: integrating color, texture, motion and shape. *International Journal of Computer Vision* 72 (2), 199–215.
- Delong, A., Boykov, Y., 2009. Globally optimal segmentation of multi-region objects. *International Conference on Computer Vision*, 285–292.
- Light, R.W., 2008. Disorders of the pleura and mediastinum. In: Fauci, A.S., Longo, D.L. (Eds.), *Harrison's Principles of Internal Medicine*, 17th ed. McGraw-Hill, pp. 1658–1661.
- Feldmar, J., Malandain, G., Declerck, J., Ayache, N., Cedex, A.S., 1996. Extension of the ICP algorithm to non rigid intensity-based registration of 3D volumes. *Computer Vision and Image Understanding* 66 (2), 193–206.
- Fornet, M., Rohr, K., Sprengel, R., Stiehl, H.S., 1998. Elastic medical image registration using orientation attributes at landmarks. *Proceedings of the Medical Image Understanding and Analysis*, 49–52.
- Freedman, D., Zhang, T., 2005. Interactive graph cut based segmentation with shape priors. *IEEE Conference on Computer Vision and Pattern Recognition* 1, 755–762.
- Funka-Lea, G., Boykov, Y., Florin, C., Jolly, M., Moreau-Gobard, R., Ramaraj, R., Rinck, D., 2006. Automatic heart isolation for CT coronary visualization using graph-cuts. *International Symposium on Biomedical Imaging*, 614–617.
- Hanaoka, S., Fritscher, K., Martin, W., Nemoto, M., Masutani, Y., Hayashi, N., Ohtomo, K., Schubert, R., 2011. 3-D graph cut segmentation with Riemannian metrics to avoid the shrinking problem. *International Conference on Medical Image Computing and Computer Assisted Intervention* 6893, 554–561.
- Heimann, T., Meinzer, H., 2009. Statistical shape models for 3D medical image segmentation: a review. *Medical Image Analysis* 13 (4), 543–563.
- Hu, S., Hoffman, E.A., Reinhardt, J.M., 2001. Automatic lung segmentation for accurate quantitation of volumetric X-ray CT images. *IEEE Transactions on Medical Image* 20 (6), 490–498.
- Hua, P., Song, Q., Sonka, M., Hoffman, E. A., Reinhardt, J.M., 2011. Segmentation of pathological and diseased lung tissue in CT images using a graph-search algorithm. *International Symposium on Biomedical Imaging*, pp. 2072–2075.
- Ishikawa, H., 2003. Exact optimization for Markov random fields with convex priors. *IEEE Transactions on Pattern Analysis and Machine Intelligence* 25 (10), 1333–1336.
- Kido, S., Tsunomori, A., 2009. Automated extraction of pleural effusion in three-dimensional thoracic CT images. In: *Medical Imaging 2009, Proceedings of the SPIE*, 7260, pp. 72600D–72600D-8.
- Lempitsky, V., Rother, C., Roth, S., Blake, A., 2010. Fusion move for Markov random field optimization. *IEEE Transactions on Pattern Analysis and Machine Intelligence* 32 (8), 1392–1405.
- Leventon, M.E., Grimson, W.E.L., Faugeras, O., 2000. Statistical shape influence in geodesic active contours. *IEEE Conference on Computer Vision and Pattern Recognition* 1, 316–323.
- Linguraru, M.G., Pura, J.A., Pamulapati, V., Summers, R.M., 2012. Statistical 4D graphs for multi-organ abdominal segmentation from multiphase CT. *Medical Image Analysis* 16 (4), 904–914.
- Rother, C., Kolmogorov, V., Lempitsky, V., Szummer, M., 2007. Optimizing binary MRFs via extended roof duality. In: *IEEE Conference on Computer Vision and Pattern Recognition*, pp. 1–8.
- Shimizu, A., Nakagomi, K., Narihira, T., Kobatake, H., Nawano, S., Shinozaki, K., Ishizu, K., Togashi, K., 2010. Automated segmentation of 3D CT images based on statistical atlas and graph cuts. In: *International Conference on Medical Image Computing and Computer Assisted Intervention, Proceedings of Workshop on Medical Computer Vision*, pp. 127–138.
- Skocaj, D., Leonardis, A., Bischof, H., 2007. Weighted and robust learning of subspace representations. *Pattern Recognition* 40 (5), 1556–1569.
- Slabaugh, G., Unal, G., 2005. Graph cuts segmentation using an elliptical shape prior. *Proceedings of the International Conference on Image Processing* 2, 1222–1225.
- Sluimer, I., Schilham, A., Prokop, M., van Ginneken, B., 2006. Computer analysis of computed tomography scans of the lung: a survey. *IEEE Transactions on Medical Image* 25 (4), 385–405.
- Sluimer, I., Prokop, M., van Ginneken, B., 2008. Toward automated segmentation of the pathological lung in CT. *IEEE Transactions on Medical Image* 24 (8), 1025–1038.
- Uchida, Y., Shimizu, A., Kobatake, H., Nawano, S., Shinozaki, K., 2010. A comparative study of statistical shape models of the pancreas. *International Journal of Computer Assisted Radiology and Surgery* 5 (1), 385–387.
- Vicente, S., Kolmogorov, V., Rother, C., 2008. Graph cut based image segmentation with connectivity priors. In: *International Conference on Computer Vision and Pattern Recognition*.
- Yao, J., Han, W., Summers, R., 2009. Computer aided evaluation of pleural effusion using chest CT images. *International Symposium on Biomedical Imaging*, pp. 241–244.